SCIENTIFIC REPORTS

OPEN

SUBJECT AREAS:
BATTERIES
MATERIALS CHEMISTRY
SYNTHESIS AND PROCESSING
SUSTAINABILITY

Received
18 April 2013

Accepted
14 May 2013

Published
29 May 2013

Correspondence and requests for materials should be addressed to Y.C. (yicui@stanford.edu)

Rice husks as a sustainable source of nanostructured silicon for high performance Li-ion battery anodes

Nian Liu[1], Kaifu Huo[2,3], Matthew T. McDowell[2], Jie Zhao[2] & Yi Cui[2,4]

[1]Department of Chemistry, Stanford University, Stanford, California 94305, USA, [2]Department of Materials Science and Engineering, Stanford University, Stanford, California 94305, USA, [3]Wuhan National Laboratory for Optoelectronics, Huazhong University of Science and Technology (HUST), Wuhan, 430074, China, [4]Stanford Institute for Materials and Energy Sciences, SLAC National Accelerator Laboratory, 2575 Sand Hill Road, Menlo Park, CA 94025, USA.

The recovery of useful materials from earth-abundant substances is of strategic importance for industrial processes. Despite the fact that Si is the second most abundant element in the Earth's crust, processes to form Si nanomaterials is usually complex, costly and energy-intensive. Here we show that pure Si nanoparticles (SiNPs) can be derived directly from rice husks (RHs), an abundant agricultural byproduct produced at a rate of 1.2×10^8 tons/year, with a conversion yield as high as 5% by mass. And owing to their small size (10–40 nm) and porous nature, these recovered SiNPs exhibits high performance as Li-ion battery anodes, with high reversible capacity (2,790 mA h g^{-1}, seven times greater than graphite anodes) and long cycle life (86% capacity retention over 300 cycles). Using RHs as the raw material source, overall energy-efficient, green, and large scale synthesis of low-cost and functional Si nanomaterials is possible.

Rice (*Oryza sativa*), first domesticated ~8,200–13,500 years ago in China[1,2], is the second-most produced crop species worldwide (7.0×10^8 metric tons/year)[3], just below corn (Fig. 1b). Rice husks, together with sugarcane bagasse, is one of the two highest-volume agricultural process residues. For every five tons of rice harvested, one ton of husk is produced, amounting to 1.2×10^8 tons of RHs per year across the globe[4]. This huge amount of waste by-product is an environmental nuisance; hence, developing uses for this waste resources is in accord with the global paradigm shift towards sustainable development. However, current applications of RHs have been limited to those with low added value, such as fertilizer additives, stockbreeding rugs, fuels, and landfilling or paving materials[5]. Discovering and recovering high-value materials from RHs is desirable. RHs burn in air to form rice husk ash; in this process, the organic matter decomposes and silica is the major remnant. Surprisingly, silica obtained in this way is relatively pure and accounts for as much as ~20% of the dry weight of the RHs[6]. Moreover, the silica within the RHs naturally exists in the form of nanoparticles[7]. As a living plant, rice absorbs silica in the form of silicic acid from soil, and the silica accumulates around cellulose micro-compartments[8–10], as illustrated in Supplementary Fig. S1. Therefore, RHs are a natural reservoir for nanostructured silica and its derivatives.

Elemental silicon has a wide range of traditional applications in metallurgy, synthesis of silicone, and in the semiconductor industry. Nanostructured silicon materials, because of their unique properties and small size, have promising applications in a range of new technologies, such as nanoelectronics[11], photonics[12], biotechnology[13–15], energy harvesting[16–18], and energy storage[19–22]. Among them, nano-Si has attracted considerable attention as a promising anode material in next generation Li-ion batteries for electric vehicles and portable electronics[23,24]. This interest is primarily due to the large theoretical specific charge storage capacity of silicon (4,200 mA h g^{-1}), which is more than ten times the theoretical capacity of conventional graphite anodes. However, silicon anode structures experience problems with fracture and pulverization that accompanies the volume changes upon Li insertion and extraction. Recent pioneering works have shown that reducing the size of silicon to the nanoscale in at least one dimension can result in effective accommodation of the strain and can even prevent fracture[19–22,25–27]. While many guidelines for designing high-performance silicon anodes have been established, the existing methods for producing nano-Si anodes are still limited to high temperature or high energy pyrolysis of silane/polysilane/halosilane precursors[28,29] or laser ablation of bulk Si[30,31] (Fig. 1a). Whereas nano-Si anodes are superior to graphite anodes in terms of performance, alternative fabrication methods that avoid the use of expensive processing are needed to produce Si anodes with comparable cost and scalability to graphite anodes.

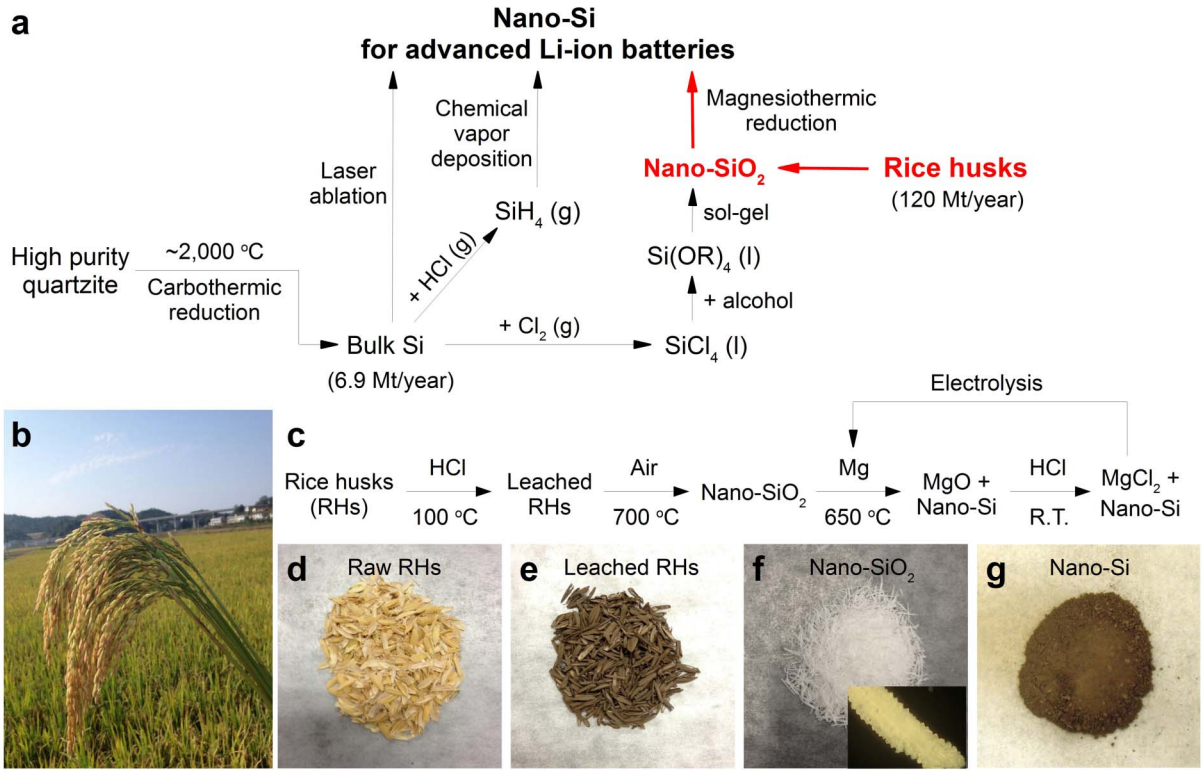

Figure 1 | A possibly low-cost, energy-efficient, green, and large scale production of nano-Si from RHs. a, Comparison between existing methods[46] and our new method (highlighted with red color) for producing nano-Si. $Si(OR)_4$ denotes silicon alkoxide. b, A panicle of ripe rice at a rice farm in China (photographed by Huo, K.). c, Flow chart of the process for recovering SiNPs from RHs. R.T. denotes room temperature. d–g, Optical images of the intermediate substances. The inset of (f) shows an optical microscopy image (0.9 mm × 0.6 mm) of one piece of heat treated RH.

We report here a method to convert RHs directly into Si nanoparticles, and demonstrate their high performance as Li-ion battery anodes. As shown in the flow chart and optical images in Fig. 1c–g, raw RHs were first converted to nano-SiO_2 by thermally decomposing the organic matter, followed by magnesiothermic reduction to produce nano-Si. Compared with the reported methods of producing nano-Si (Fig. 1a), our method has several advantages: (i) the recovered silicon inherits the intrinsic and unique nanostructure of the silica in RHs, which allows for excellent battery performance by mitigating pulverization; (ii) RHs are an abundant and sustainable materials source with a supply that far exceeds the demand for LIB anode materials; (iii) the overall method is simple, energy-efficient, and easy to scale-up; and (iv) the overall process does not use expensive Si precursors or reagents. Mg metal, one of the most commonly used structural metals, is produced by electrolytic process or Pidgeon process with a relatively low cost compared to other nano-Si precursors. And Mg can be regenerated from the $MgCl_2$ byproduct by electrolysis as shown in Fig. 1c. Thus, the whole process only consumes HCl and converts it to Cl_2 after the electrolysis. The overall process is green.

Results

Synthesis and characterization of nano-Si from RH. Preserving the nanostructure of the SiO_2 species in the RHs during the whole recovery process, especially at steps involving elevated temperature, is key to producing high quality nano-Si. In the step of converting RHs to nano-SiO_2, simply burning RHs in air will produce bulk SiO_2, and it is necessary to first perform HCl leaching[7] and then only heat at moderate temperatures to avoid the fusion of the SiO_2 product (Fig. 2a–c) while removing the organic matter. Thermogravimetric analysis (TGA) of both raw and leached RHs (Fig. 2d) shows a typical three-stage mass loss in simulated air: (i) mass loss below 100°C, which corresponds to water loss; (ii) mass loss around 300°C, which corresponds to cellulose/hemicellulose/lignin degradation; and (iii) mass loss between 350–550°C, corresponding to the burning of carbonous residues[32]. 23% of the mass remains as the SiO_2 product. Differential thermal analysis (DTA, Fig. 2e) confirms these three stages during heating, with an additional endothermic peak for the raw RH sample at 635°C (highlighted in the black square in Fig. 2e). This peak is due to the melting of silica catalyzed by metal impurities (such as K^+, Na^+, and Ca^{2+}) in raw RHs[7] and and formation of bulk SiO_2, as shown in Fig. 2a. After optimization, heating leached RHs at 700°C in air produces amorphous SiO_2 nanoparticles with diameters distributed around 80 nm; these nanoparticles are loosely interconnected and are macroscopically preserved in the shape of the RHs (Fig. 2f and Supplementary Fig. S2). In the next step, this type of nano-SiO_2 is further reduced to obtain nano-Si.

Bulk Si is usually produced for industrial applications by the carbothermic reduction of silica, which requires temperatures greater than 2000°C[33], which are well above the melting point of silicon (1410°C). When using magnesium as a reducing agent, the reaction temperature could decrease to 650°C, allowing the possibility of nanostructure preservation during silicon formation[34]. The reactions occur as below:

$$2Mg(g) + SiO_2(s) \rightarrow 2MgO(s) + Si(s),\ \Delta H = -546.42\ kJ\ mol^{-1} \quad (1)$$

or

$$2Mg(s) + SiO_2(s) \rightarrow 2MgO(s) + Si(s),\ \Delta H = -291.62\ kJ\ mol^{-1} \quad (2)$$

If Mg is in excess,

$$2Mg(g) + Si(s) \rightarrow Mg_2Si(s),\ \Delta H = -318.91\ kJ\ mol^{-1} \quad (3)$$

After reaction, MgO, Mg_2Si and unreacted Mg is removed by hydrochloric acid, yielding silicon product. In these reactions, magnesium (b.p. = 650°C) functions as a reducing agent. Previously, the

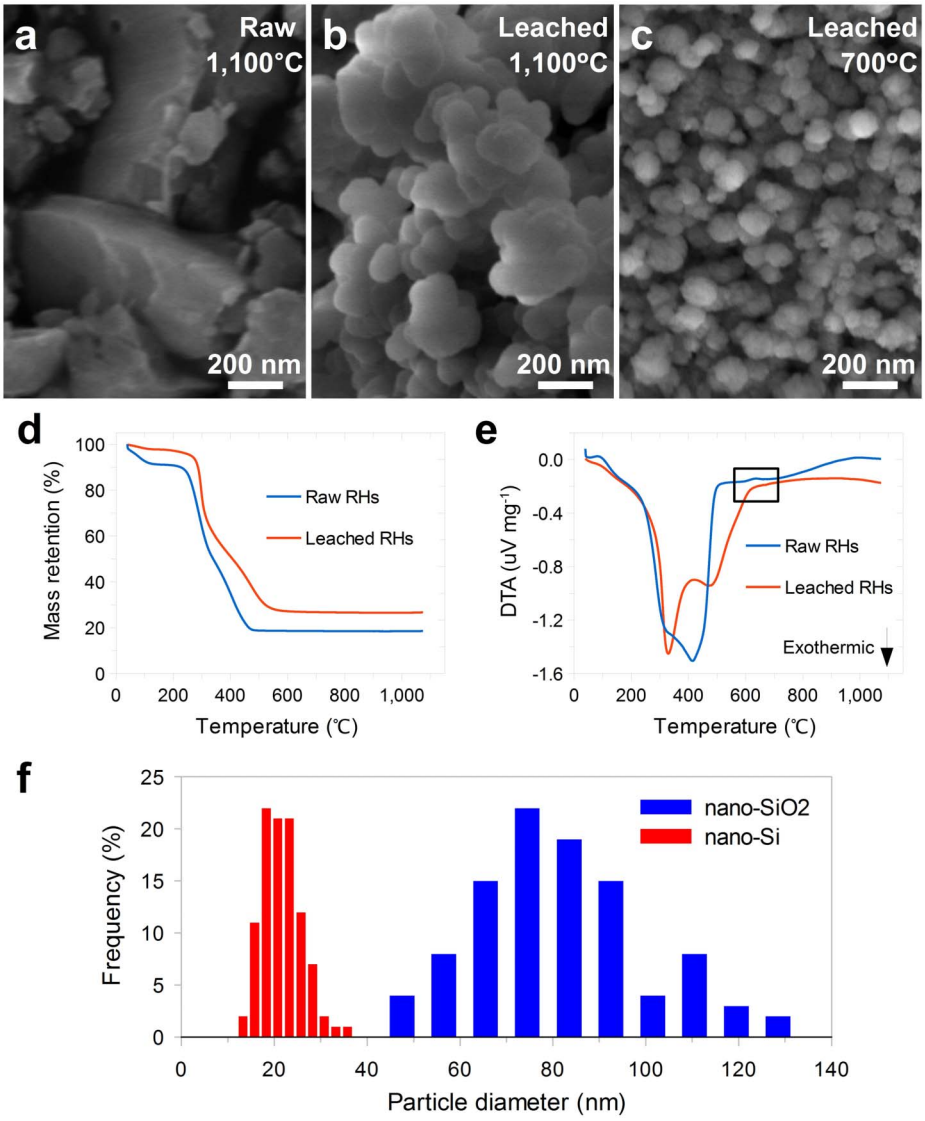

Figure 2 | Characterization of nano-SiO_2 derived from RHs. a–c, SEM images of SiO_2 obtained by heating raw or leached RHs at different temperature. d,e, TGA (d) and DTA (e) profiles of raw and leached RHs measured under flow of simulated air (20% O_2 in Ar) with a ramp rate of 5°C min^{-1}. f, Statistical analysis of particle sizes of nano-SiO_2 shown in (c) and nano-Si (Si-RH-5) reduced from it.

Mg and SiO_2 reactants were placed at separate locations, and Mg vapor diffuses to react with SiO_2[34]. Upon testing, this configuration limited the yield and scalability, because the Si product near the Mg source was further converted to Mg_2Si (reaction (3)), while the SiO_2 far from Mg source was not reduced. Instead, we conduct the reaction with Mg and SiO_2 powder premixed together to increase the scalability and yield. Both reactions (1) and (2) takes place in this configuration, because Mg powder is in direct contact with SiO_2, and the Mg has high enough vapor pressure at elevated temperature (e.g. 1 Pa at 428°C). In a closed reactor (Supplementary Fig. S3), a slight excess of Mg (Mg : SiO_2 molar ratio = 2.5 : 1) was added, so that there would neither be a lack of Mg owing to Mg vapor escaping nor a large excess of Mg to convert Si to Mg_2Si. We found that the temperature ramp rate significantly affects the morphology of the product. Macroporous Si was obtained with a 40°C min^{-1} rate (sample Si-RH-40, Fig. 3a and Supplementary Fig. S4), while partially interconnected Si nanoparticles were obtained with a 5°C min^{-1} rate (sample Si-RH-5, Fig. 3b–d, and Supplementary Fig. S5). XRD patterns of products before (Supplementary Fig. S6) and after HCl treatment (Fig. 3e) showed that the 40°C min^{-1} sample had sharper peaks from Si and MgO, confirming larger grain sizes. Nitrogen adsorption (Brunauer-Emmett-Teller, BET) measurements (Fig. 3f and Supplementary Table S1) indicate that the specific surface area of the starting nano-SiO_2 was 289 m^2 g^{-1}; this value decreased dramatically to 54 m^2 g^{-1} for sample Si-RH-40 and only slightly to 245 m^2 g^{-1} for sample Si-RH-5. BJH (Barrett-Joyner-Halenda) analysis further revealed that the Si-RH-5 sample has significant pores less than 10 nm in size, while the Si-RH-40 sample has negligible porosity with size less than 20 nm. The different characteristics of Si produced at different temperature ramp rates can be understood by local heat accumulation. Due to the large negative enthalpies associated with magnesiothermic reduction, a large amount of heat is released in local areas. With a fast ramp rate, little time is allowed for heat radiation or conduction to occur, so local temperature increases accelerate nearby reactions, which further increases the local temperature. These high temperatures cause the fusion of Si products and the disappearance of small pores. At the same time, Si coats and fuses around the MgO that forms, and after dissolving MgO with HCl, macroporous Si remains (Fig. 3a). In sample Si-RH-40, some MgO might be completely coated with Si so that HCl cannot access it during etching, which is why relatively intense MgO peaks appear in the XRD pattern of Si-RH-40 (Fig. 3e). Another

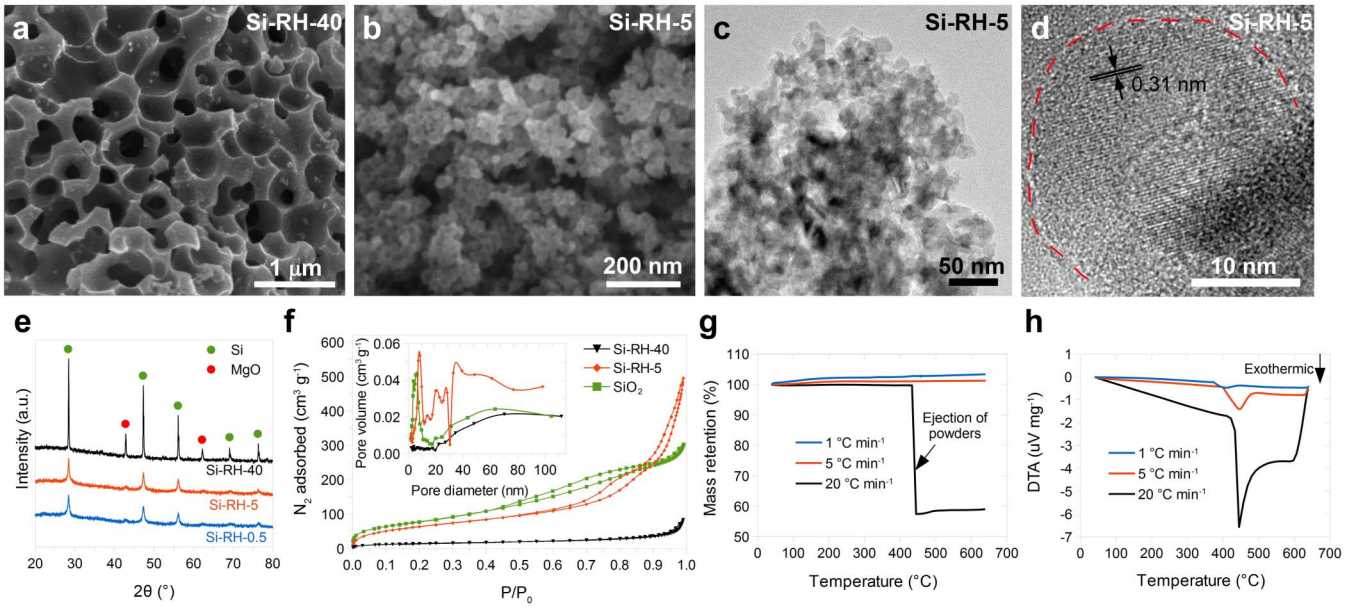

Figure 3 | Conversion of nano-SiO_2 to nano-Si and characterization. a,b, SEM images of nano-Si obtained by magnesiothermic reduction of nano-SiO_2 with ramp rates of 40°C min^{-1} (a) and 5°C min^{-1} (b). c,d, TEM images of Si-RH-5 with different magnifications. The high-resolution TEM image (d) shows one spherical SiNP and the (111) lattice spacing of crystalline Si is clearly visible (the red line indicates the boundary of the SiNP). e, XRD patterns of Si obtained by magnesiothermic reduction of nano-SiO_2 with ramp rates of 40, 5, and 0.5°C min^{-1} from 400°C to 650°C (after HCl treatment). f, N_2 adsorption-desorption isotherms of nano-SiO_2 and the Si samples reduced from it. Inset, pore size distribution. g,h, TGA (g) and DTA (h) profiles of the reaction between nano-SiO_2 and Mg with different ramp rates under inert atmosphere.

result of this violent inhomogeneous reaction was the formation of Mg_2Si in Si-RH-40 (Supplementary Fig. S6).

TGA and DTA were employed to further investigate this reaction. The mass of the mixture did not change during the reaction with a slow ramp rate (Fig. 3g). With a higher ramp rate (20°C min^{-1}), however, the powders were ejected out of the TGA crucible at 433°C, indicating a violent reaction. DTA directly shows that the reaction occurs around 400–450°C, and that the higher ramp rate results in more severe heat accumulation (Fig. 3h), which ultimately leads to the violent reaction and ejection of reactants. Therefore, in order to obtain nano-Si, a slower heating rate of about 5°C min^{-1} is necessary. Further decreasing the heating rate from 5 to 0.5°C min^{-1} does not decrease the particle size or influence the crystallinity. The obtained Si nanoparticles (Si-RH-5) have sizes around 22 nm (Fig. 2f, Fig. 3c–d). Theoretically, spherical 22 nm single crystalline Si particles have a specific surface area of 117 m^2 g^{-1}, which is only half of the measured value (Supplementary Table S1). Hence, the Si nanoparticles obtained here are porous, which is consistent with the pore diameter analysis (Fig. 3f, inset). This naturally-inherited porous nanoparticle morphology meets the requirement of a stable Si anode to accommodate the volume change induced by lithium insertion/extraction (discussed below).

The electrical response of a pellet of nano-Si was tested, and it exhibited ohmic I-V characteristics (Supplementary Fig. S7). The metallic nature of the nano-Si suggests the existence of impurities. The relatively low conductivity of 3.0×10^{-3} S m^{-1} could be due to the native oxide on the nanoparticles, which decreases the interparticle conductivity. To quantitatively examine the purity of the Si product, secondary ion mass spectroscopy (SIMS), which has sub-parts-per-million sensitivity, was used. The nano-Si pellet was subjected to a primary O^- ion beam and secondary ions were ejected. Six metals common to biological systems (Na, Mg, Al, K, Ca, and Fe), together with Si, were detected simultaneously by the mass spectrometer. The Si purity is determined to be higher than 99.6% based on the trace metal concentrations (Supplementary Fig. S8). The impurity with the highest concentration (less than 0.3%) is Mg. Most of the Mg is probably introduced during the magnesiothermic reduction. The element with the second highest impurity concentration was Fe (less than 0.07%). Na, Ca, K, and Al were all under 0.01%. Although the nano-Si is directly recovered from a natural substance, its purity is more than enough for application in Li-ion battery anodes. The impurities may even improve the electrical conductivity of the Si anode through doping. For other applications, such as solar cells, the impurity level must be much lower, which could possibly be realized with a purer Mg reagent and additional acid leaching of the RH and the mixture after the magnesiothermic reduction[6]. It should be noted that previous attempts to recover silicon from RHs focused on the purity, because the purpose was to use them in solar cells[35]. Here, we focus primarily on preserving the nanostructure of the recovered silicon, targeting application in Li-ion batteries.

Electrochemical behavior of nano-Si from RH. Unlike bulk Si, the recovered nano-Si has high functionality due to the small size and porous nature. It exhibits excellent electrochemical behavior without any further coating or modification (Fig. 4). Upon deep galvanostatic cycling between 0.01 and 1 V, the discharge (delithiation) capacity reaches 2790 mA h g^{-1} for the first cycle at C/50 and stabilizes around 1750 mA h g^{-1} for later cycles at C/2 (Fig. 4a); these values are seven and five times the theoretical capacity of graphite (372 mA h g^{-1}). The cycling stability is excellent as well. No capacity decay was observed over the 150 cycles after the initial lower-current cycles, and the capacity retention values after 200 and 300 cycles are 95% and 86%, respectively. The voltage profiles for the different cycles are shown in Supplementary Fig. S9. The similarity of the profiles over 300 cycles indicates highly reversible Li insertion and extraction.

Cyclic voltammetry experiments (CV, Fig. 4b) show lithiation and delithiation peaks at potentials typical of the reaction of Si[21]. An activation process occurred over the first few cycles, as indicated by the increase of the CV peak intensity and a decrease of the charge transfer resistance measured by impedance spectroscopy (Supplementary Fig. S10). To study the electrode morphology after activation, the cell was disassembled after 60 cycles to observe the nano-Si

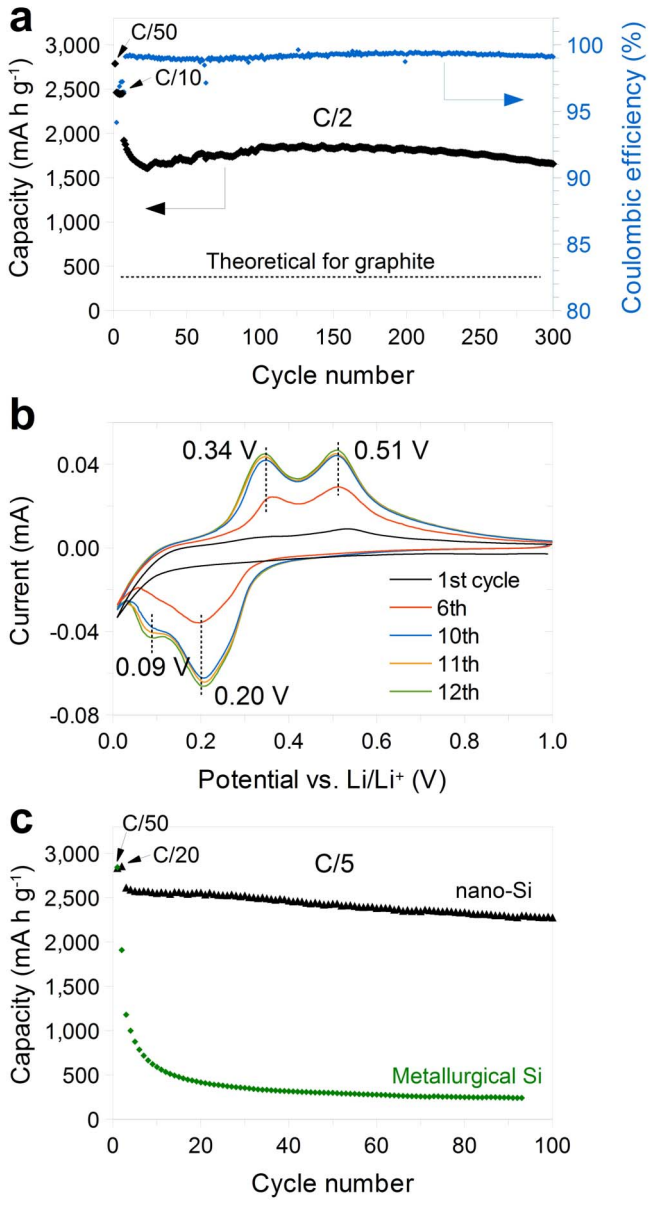

Figure 4 | Li-ion battery anode using nano-Si recovered from RHs. a, Delithiation capacity and Coulombic efficiency (CE) of the first 300 galvanostatic cycles. The rate was C/50 for the first cycle, then C/10 for 5 cycles, and C/2 for the later cycles. b, Cyclic voltammogram (CV) versus Li/Li^+ at a 0.02 mV s^{-1} scan rate. Selected cycles are shown for clarity. c, Galvanostatic cycling of nano-Si recovered from RHs and commercial metallurgical-grade Si particles. Both electrodes were cycled at C/50 for the first cycle, C/20 for the second cycle, and C/5 for the later cycles. All the nano-Si electrodes in a–c were tested between 1 V and 0.01 V versus Li/Li^+ with PVDF binder. 1C = 4.2 A g^{-1} Si.

with SEM. The nano-Si still showed high porosity, but the initial nanoparticles evolved into nanoporous frameworks (Supplementary Fig. S11b–c). Two processes could have happened during activation. First, the viscous flow of Li_xSi during lithiation/delithiation could result in morphology changes[36]. Second, it may take a few cycles for the native oxide on the surface of each Si particle to become lithiated and conductive for Li^+. We therefore always applied a low current density in the first few galvanostatic cycles for thorough activation of nano-Si. After ten CV cycles, the profiles became stable, meaning that activation is finished (Fig. 4b) and the electrode fully reacts. This in situ tune-up of morphology during the activation process increases the interparticle conductivity, shorten the Li diffusion pathway, and therefore improves the kinetics of the nano-Si anode. After activation, the nano-Si anode can deliver a reversible capacity of 1120 mA h g^{-1} at 1C (4.2 A g^{-1}) and 644 mA h g^{-1} at 2C (8.4 A g^{-1}) rates, respectively (Supplementary Fig. S12). Moreover, the high internal porosity enables the volume expansion of Si without rupturing the solid-electrolyte interphase (SEI) at the outer surface. Instead of repetitively breaking and reforming SEI during extended cycling, a thin and stable SEI conformally covers the surface of the nano-Si electrode (Supplementary Fig. S11a), which results in high reversibility and therefore good cycling stability[22,37]. Coulombic efficiency (CE), an indicator of SEI formation and stability in anodes, is as high as 99.3% when averaged from the 100th to the 300th cycle (Fig. 4a). The first cycle CE is ~70% because the initial SEI formation and the lithiation of the native oxide consumes some lithium; this value could be increased by performing prelithiation[38].

Discussion

The capacity, cycle life and CE of nano-Si anodes were achieved without any further material modification, such as surface coating. And we used standard polyvinylidene fluoride (PVDF) binder, regarded to be poor for Si anodes, for all the electrochemical tests. With PVDF, commercial ~100 nm SiNPs lose over 50% of the capacity within only 5 cycles[21]. Instead, the small size (10–40 nm) and porous nature of the RH derived nano-Si effectively accommodated the volume change of Si and improve the stability significantly. And we expected that surface coatings[39,40], or binders such as sodium alginate[21], polyacrylic acid[41], and conducting polymer[42] can further improve the performance of the nano-Si anodes.

To the best of our knowledge, the only other Si material that has similar scalability and cost is metallurgical-grade Si. It is made up of micron-sized powders with ~98% purity produced by carbothermic reduction from quartzite at ~2000°C, as shown in Fig. 1a. The particle size are big due to the melting of Si during the high temperature process. We compared its battery performance with the nano-Si recovered from RHs (Fig. 4c). After only 20 cycles, the capacity of the metallurgical-grade Si drops below 500 mA h g^{-1}, while RH-derived nano-Si still delivers 2200 mA h g^{-1} after 100 cycles. Therefore, the nano-Si synthesized by our method has superior battery performance together with scalable production and low cost. In addition, the nano-Si anodes derived from RHs, without any coating, have better cycling stability and longer cycle life than those derived from other silica sources, such as diatomaceous earth[43] and synthesized nanostructured silica[40,44,45], with either carbon or silver coating (Fig. 1a). The small size, high porosity and interconnectedness of the nano-Si derived from RHs are the key to achieve such high performance. The unique morphology is inherited by the natural silica nanoparticles in RHs and the successful preservation of the nanostructure throughout the recovery process.

Unlike other long cycle life and high capacity nanostructured Si anodes[21,22,37], the nano-Si here is derived without any use of energy-intensive processes such as silane CVD or laser ablation. Our approach uses abundant and sustainable source: rice husks. The Mg metal reducing reagent can be regenerated through electrolysis and thus the whole process is green. Moreover, the method here has superior scalability to other nano-Si fabrication processes. For a demonstration in laboratory, we increased the size of our reaction and recover one gram of nano-Si from RHs (Supplementary Fig. S13).

In summary, whereas silicon nanomaterials have found potential application in a number of areas, green, cost-effective, and scalable synthesis of them from sustainable sources still remained challenging. To conquer this barrier, we developed a route of recovering nano-Si directly from rice husks, an agricultural waste, in which silicon naturally exists in the form of silica nanoparticles. By coping with the strongly exothermic reactions, we succeeded in preserving the

nanostructure of silicon. Moreover, the uniquely small size and porous nature of the obtained nano-Si gives it superior performance as Li-ion battery anode, over both commercial metallurgical-grade silicon particles and commercial non-porous silicon nanoparticles. And the simplicity, cost effectiveness, and scalability of the fabrication process make our RH-derived nano-Si anode promising for next generation Li-ion batteries. In addition to Li-ion batteries, the plentiful potential large-scale application of nanostructured Si renders tremendous opportunities for this kind of agricultural byproduct derived nanomaterial.

Methods

Recovery of nano-Si from RHs. 3 g of RHs (Farmers' Rice Co., USA) were first refluxed with 45 mL of 10% HCl for 2 h to remove the metal ions inside. The leached RHs were collected by filtration, washed with a large amount of deionized water, dried at 100°C, and heated in air at 700°C for 2 h with a ramp rate of 5°C min^{-1}. A white nano-SiO_2 remnant formed with a yield about 0.5 g.

100 mg of the obtained nano-SiO_2 was thoroughly ground along with 100 mg of Mg powder (~325 mesh, 99.8%, Alfa Aesar) and sealed in a 5/8 in. Swagelok brass union capped with two 5/8 in. Swagelok stainless steel plugs (Supplementary Fig. S3) inside an Ar-filled glovebox. The powders were spread evenly at the bottom of the horizontal reactor to avoid local heat accumulation during the exothermic reaction. The reactor was heated inside a tube furnace under H_2 or inert gas flow to 400°C over 10 min, then it was heated to 650°C with a ramp rate of 5°C min^{-1}, and finally it was held at 650°C for 2 h. After this process, the reactor was taken out of the furnace when the temperature fell below 100°C. The obtained powders were soaked in 1 M HCl solution (molar ratio of HCl : H_2O : EtOH = 0.66 : 4.72 : 8.88) for 6 h to remove MgO and Mg_2Si and then they were soaked in 5% hydrofluoric acid for 10 min to ensure that any unreacted or newly formed SiO_2 was removed. No difference were noticed without HF etching. After drying under vacuum at room temperature, nano-Si powders were obtained with a yield of about 30 mg.

Characterization. TGA/DTA measurements (Netzsch STA 449) were carried out under Ar or simulated air atmosphere (20% O_2 in Ar, both are 99.99% pure gases from Airgas). The heating rate is 5°C min^{-1} if not specified. Other characterization was carried out using SEM (FEI Nova NanoSEM), TEM (FEI Tecnai G2 F20 X-twin), XRD (PANalytical X'Pert, Ni-filtered Cu Kα radiation), and nitrogen adsorption-desorption measurement (Micromeritics, ASAP 2020). Before nitrogen adsorption measurements, the samples were degassed at 200°C under high vacuum for 10 h. Secondary ion mass spectroscopy (Cameca NanoSIMS 50 L) was used to measure the trace impurities in SiNPs from RHs. The SiNPs were tightly roll-pressed onto a Cu foil to form a 10 μm thick pellet (Fig. 4a). A primary O^- ion beam (16 keV impact energy, normal to the surface) was applied to analyze the positive secondary ions emitted from the SiNP film. The rastered area of the primary ion beam was 20 μm × 20 μm while the gating area was 1.3 μm × 1.3 μm. The sputtering rate was ~0.2 nm min^{-1}. Seven secondary ion masses, corresponding to ^{23}Na,^{24}Mg,^{27}Al,^{28}Si,^{39}K,^{44}Ca, and ^{56}Fe were detected simultaneously and corrected with the natural abundance of isotopes.

Electrochemistry. To prepare electrodes, a mixture of 65% wt/wt nano-Si, 20% wt/wt carbon black (Super P, TIMCAL, Switzerland), and 15% wt/wt polyvinylidene fluoride (Kynar HSV 900) was ground to form homogeneous, black powders. A slurry containing this mixture in 1-methyl-2-pyrrolidinone (NMP) was spread onto a thin copper foil and dried. The Si mass loading is typically 0.1–0.2 mg/cm^2. Prior to cell fabrication, the electrodes were heated in a vacuum oven at 60°C for at least 2 h. Coin-type cells (2032) were fabricated inside an Ar-filled glovebox with the nano-Si working electrode, a Li metal foil counter/reference electrode, and a Celgard 2250 separator soaked in electrolyte. The electrolyte is 1.0 M $LiPF_6$ in 1 : 1 w/w ethylene carbonate/diethyl carbonate (EMD Chemicals). 1 vol % vinylene carbonate (Novolyte Technologies) was added to the electrolyte to improve the cycling stability. Cyclic voltammetry and electrochemical impedance spectroscopy measurements were carried out on a BioLogic VMP3 system. Galvanostatic cycling was done using an MTI 8 Channels battery tester. If not mentioned otherwise, the voltage cutoffs are 0.01 and 1 V vs Li/Li^+. The specific capacity is calculated based on the mass of Si. The charge/discharge rate was calculated assuming the theoretical capacity of Si (4,200 mA h g^{-1}). The Coulombic efficiency was calculated as $C_{dealloy}/C_{alloy}$, where $C_{dealloy}$ and C_{alloy} are the capacity of the anodes during Li extraction and insertion. Electrodes with metallurgical-grade Si (Alfa Aesar, crystalline, 100–200 mesh, 98%) were fabricated in the same manner and tested for comparison with the recovered nano-Si from RHs.

To characterize the electrodes after cycling, cells were charged to 1 V and opened. The nano-Si electrodes were soaked in acetonitrile to remove the electrolyte. To remove the SEI, electrodes were further soaked in 0.5 M HCl and rinsed with deionized water.

1. Huang, X. *et al.* A map of rice genome variation reveals the origin of cultivated rice. *Nature* **490**, 497–501 (2012).
2. Molina, J. *et al.* Molecular evidence for a single evolutionary origin of domesticated rice. *Proc. Natl. Acad. Sci. USA* **108**, 8351–8356 (2011).
3. Food and Agriculture Organization (FAO) of the United Nations (2010).
4. Tuck, C. O., Pérez, E., Horváth, I. T., Sheldon, R. A. & Poliakoff, M. Valorization of biomass: deriving more value from waste. *Science* **337**, 695–699 (2012).
5. Shackley, S. *et al.* Sustainable gasification–biochar systems? A case-study of rice-husk gasification in Cambodia, Part I: Context, chemical properties, environmental and health and safety issues. *Energy Policy* **42**, 49–58 (2012).
6. Sun, L. & Gong, K. Silicon-based materials from rice husks and their applications. *Ind. Eng. Chem. Res.* **40**, 5861–5877 (2001).
7. Wang, W. *et al.* Silica nanoparticles and frameworks from rice husk biomass. *ACS Appl. Mater. Interfaces* **4**, 977–981 (2011).
8. Ma, J. F. *et al.* A silicon transporter in rice. *Nature* **440**, 688–691 (2006).
9. Currie, H. A. & Perry, C. C. Silica in plants: biological, biochemical and chemical studies. *Annals of Botany* **100**, 1383–1389 (2007).
10. Tabata, S., Iida, H., Horie, T. & Yamada, S. Hierarchical porous carbon from cell assemblies of rice husk for in vivo applications. *Med Chem Comm* **1**, 136–138 (2010).
11. Cui, Y. & Lieber, C. M. Functional nanoscale electronic devices assembled using silicon nanowire building blocks. *Science* **291**, 851–853 (2001).
12. Pavesi, L., Dal Negro, L., Mazzoleni, C., Franzo, G. & Priolo, F. Optical gain in silicon nanocrystals. *Nature* **408**, 440–444 (2000).
13. Lin, V. S.-Y., Motesharei, K., Dancil, K.-P. S., Sailor, M. J. & Ghadiri, M. R. A porous silicon-based optical interferometric biosensor. *Science* **278**, 840–843 (1997).
14. Park, J.-H. *et al.* Biodegradable luminescent porous silicon nanoparticles for in vivo applications. *Nature Mater.* **8**, 331–336 (2009).
15. Tian, B. *et al.* Three-dimensional, flexible nanoscale field-effect transistors as localized bioprobes. *Science* **329**, 830–834 (2010).
16. Tian, B. *et al.* Coaxial silicon nanowires as solar cells and nanoelectronic power sources. *Nature* **449**, 885–889 (2007).
17. Hochbaum, A. I. *et al.* Enhanced thermoelectric performance of rough silicon nanowires. *Nature* **451**, 163–167 (2008).
18. Boukai, A. I. *et al.* Silicon nanowires as efficient thermoelectric materials. *Nature* **451**, 168–171 (2008).
19. Chan, C. K. *et al.* High-performance lithium battery anodes using silicon nanowires. *Nature Nanotech.* **3**, 31–35 (2008).
20. Magasinski, A. *et al.* High-performance lithium-ion anodes using a hierarchical bottom-up approach. *Nature Mater.* **9**, 353–358 (2010).
21. Kovalenko, I. *et al.* A major constituent of brown algae for use in high-capacity Li-ion batteries. *Science* **75**, 75–79 (2011).
22. Wu, H. *et al.* Stable cycling of double-walled silicon nanotube battery anodes through solid-electrolyte interphase control. *Nature Nanotech.* **7**, 310–315 (2012).
23. Hatchard, T. D. & Dahn, J. R. In situ XRD and electrochemical study of the reaction of lithium with amorphous silicon. *J. Electrochem. Soc.* **151**, A838–A842 (2004).
24. Obrovac, M. N. & Krause, L. J. Reversible Cycling of Crystalline Silicon Powder. *J. Electrochem. Soc.* **154**, A103 (2007).
25. Liu, X. H. *et al.* Size Dependent Fracture of Silicon Nanoparticles During Lithiation. *ACS Nano* **6**, 1522–1531 (2012).
26. Lee, S. W., McDowell, M. T., Berla, L. A., Nix, W. D. & Cui, Y. Fracture of crystalline silicon nanopillars during electrochemical lithium insertion. *Proc. Natl. Acad. Sci. USA* **109**, 4080–4085 (2012).
27. Wu, H. & Cui, Y. Designing nanostructured Si anodes for high energy lithium ion batteries. *Nano Today* **7**, 414–429 (2012).
28. Cui, Y., Lauhon, L. J., Gudiksen, M. S., Wang, J. & Lieber, C. M. Diameter-controlled synthesis of single-crystal silicon nanowires. *Appl. Phys. Lett.* **78**, 2214 (2001).
29. Law, M., Goldberger, J. & Yang, P. Semiconductor nanowires and nanotubes. Annu. Rev. *Mater. Res.* **34**, 83–122 (2004).
30. Morales, A. M. & Lieber, C. M. A laser ablation method for the synthesis of crystalline semiconductor nanowires. *Science* **279**, 208–211 (1998).
31. Geohegan, D. B., Puretzky, A. A., Duscher, G. & Pennycook, S. J. Time-resolved imaging of gas phase nanoparticle synthesis by laser ablation. *Appl. Phys. Lett.* **72**, 2987 (1998).
32. Wang, W. *et al.* Harvesting silica nanoparticles from rice husks. *J. Nanoparticle Res.* **13**, 6981–6990 (2011).
33. Nagamori, M., Malinsky, I. & Claveau, A. Thermodynamics of the silicon-carbon-oxygen system for the production of silicon carbide and metallic silicon. *Metall. Trans. B* **17**, 503–514 (1986).
34. Bao, Z. *et al.* Chemical reduction of three-dimensional silica micro-assemblies into microporous silicon replicas. *Nature* **446**, 172–175 (2007).
35. Banerjee, H. D., Sen, S. & Acharya, H. N. Investigations on the production of silicon from rice husks by the magnesium method. *Mater. Sci. Eng.* **52**, 173–179 (1982).
36. Gu, M. *et al.* In situ TEM study of lithiation behavior of silicon nanoparticles attached to and embedded in a carbon matrix. *ACS Nano* **6**, 8439–8447 (2012).
37. Liu, N. *et al.* A yolk-shell design for stabilized and scalable Li-ion battery alloy anodes. *Nano Lett.* **12**, 3315–3321 (2012).
38. Liu, N., Hu, L., McDowell, M. T., Jackson, A. & Cui, Y. Prelithiated silicon nanowires as an anode for lithium ion batteries. *ACS Nano* **5**, 6487–6493 (2011).
39. Kasavajjula, U., Wang, C. & Appleby, A. J. Nano- and bulk-silicon-based insertion anodes for lithium-ion secondary cells. *J. Power Sources* **163**, 1003–1039 (2007).

40. Yu, Y. *et al*. Reversible storage of lithium in silver-coated three-dimensional macroporous silicon. *Adv. Mater.* **22**, 2247–2250 (2010).
41. Magasinski, A. *et al*. Toward efficient binders for Li-ion battery Si-based anodes: polyacrylic acid. *ACS Appl. Mater. Interfaces* **2**, 3004–3010 (2010).
42. Liu, G. *et al*. Polymers with tailored electronic structure for high capacity lithium battery electrodes. *Adv. Mater.* **23**, 4679–4683 (2011).
43. Shen, L., Guo, X., Fang, X., Wang, Z. & Chen, L. Magnesiothermically reduced diatomaceous earth as a porous silicon anode material for lithium ion batteries. *J. Power Sources* **213**, 229–232 (2012).
44. Jia, H. *et al*. Novel three-dimensional mesoporous silicon for high power lithium-ion battery anode material. *Adv. Energy Mater.* **1**, 1036–1039 (2011).
45. Chen, D. *et al*. Reversible Lithium-Ion Storage in Silver-Treated Nanoscale Hollow Porous Silicon Particles. *Angew. Chem. Int. Ed.* **51**, 2409–2413 (2012).
46. Simmler, W. Silicon Compounds, Inorganic. Ullmann's Encyclopedia of Industrial Chemistry (2000). doi:10.1002/14356007.a24_001.

Acknowledgements

We thank Farmers' Rice Corp. for providing the rice husks. We thank Sangmoo Jeong for the help with electrical conductivity measurement and Chuck Hitzman for the help with SIMS measurement. Part of this research was conducted using the Cameca NanoSIMS 50 L, supported by the NSF under award # 0922648. Y.C. acknowledges the support from the Assistant Secretary for Energy Efficiency and Renewable Energy, Office of Vehicle Technologies of the U.S. Department of Energy under Contract No. DE-AC02-05CH11231, Subcontract No. 6951379 under the Batteries for Advanced Transportation Technologies (BATT) Program. K.H. acknowledges the financial support of the China Scholarship Council (CSC) (No.2008601301). M.T.M. acknowledges the National Science Foundation Graduate Fellowship Program and the Stanford Graduate Fellowship Program.

Author contributions

N.L., K.H. and Y.C. conceived the concept of recovering Si from rice husks for Li-ion batteries. N.L. developed and carried out the fabrication of Si, conducted materials characterization and electrochemical measurements. M.T.M. conducted TEM characterization. J.Z. conducted gram-scale fabrication. N.L., K.H., M.T.M. and Y.C. co-wrote the paper. All authors discussed the results and commented on the manuscript.

Additional information

Supplementary information accompanies this paper at http://www.nature.com/scientificreports

Competing financial interests: The authors declare no competing financial interests.

How to cite this article: Liu, N., Huo, K.F., McDowell, M.T., Zhao, J. & Cui, Y. Rice husks as a sustainable source of nanostructured silicon for high performance Li-ion battery anodes. *Sci. Rep.* **3**, 1919; DOI:10.1038/srep01919 (2013).